Biosensors and Bioelectronics 259 (2024) 116387

Contents lists available at ScienceDirect

Biosensors and Bioelectronics

journal homepage: www.elsevier.com/locate/bios

Self-powered photoelectrochemical aptasensor for fumonisin B1 detection based on a Z-scheme $ZnIn_2S_4/WO_3$ photoanode

Xiang Ren [a], Jingui Chen [a,**], Xiance Gan [a], Na Song [a], Xiaoran Yang [a], Jinxiu Zhao [b,***], Hongmin Ma [a], Huangxian Ju [c], Qin Wei [a,d,*]

[a] Key Laboratory of Chemical Sensing & Analysis in Universities of Shandong, School of Chemistry and Chemical Engineering, University of Jinan, Jinan 250022, China
[b] School of Materials Science and Engineering, University of Jinan, Jinan 250022, China
[c] State Key Laboratory of Analytical Chemistry for Life Science, School of Chemistry and Chemical Engineering, Nanjing University, Nanjing 210023, China
[d] Department of Chemistry, Sungkyunkwan University, Suwon, 16419, Republic of Korea

ARTICLE INFO

Keywords:
Photoelectrochemical
Self-powered
$ZnIn_2S_4/WO_3$
Au@W–Co_3O_4
Fumonisin B1

ABSTRACT

The incidence of esophageal cancer is positively associated with fumonisin contamination. It is necessary to develop methods for the rapid detection of fumonisins. In this work, a self-powered photoelectrochemical aptamer sensor based on $ZnIn_2S_4/WO_3$ photoanode and Au@W–Co_3O_4 photocathode is proposed for the sensitive detection of fumonisin B1 (FB1). Among them, under visible light irradiation, the Z-type heterostructure of $ZnIn_2S_4/WO_3$ acts as a photoanode to improve the electron transfer rate, which contributes to the enhancement of the photocathode signal and lays the foundation for a wider detection range. The Au@W–Co_3O_4 photocathode as a sensing interface reduces the probability of false positives (comparison of anode sensing platforms). The PEC sensor has a good working performance in the detection range (10 pg/mL-1000 ng/mL) with a detection limit of 2.7 pg/mL (S/N = 3). In addition, the sensor offers good selectivity, stability and excellent recoveries in real sample analysis. This work is expected to play a role in the field of analyzing environmental toxins.

1. Introduction

Fumonisin is a metabolite produced by fusarium stringers, of which FB1 is strongly associated with the development of esophageal cancer (Wei et al., 2023; Mao et al., 2019). Therefore, designing a simple, stable, reliable, and rapid FB1 detection method is an important way to ensure human health. In recent years, photoelectrochemistry (PEC) has developed rapidly due to its advantages of high sensitivity, low background signal, and low detection limit, and has been used for the detection of various environmental pollutants and cancer markers (Shu and Tang, 2020; Govindaraju et al., 2016). The PEC detection system adopts a three-electrode mode, in which the photoanode and photocathode are more common as working electrodes (Zhao and Ding, 2019; Zang et al., 2018). The photoanode composed of n-type semiconductor has a strong photocurrent response, but there is a false-positive problem in the detection process (Zhu et al., 2021; Sun et al., 2022). The photocathode composed of p-type semiconductor solves the problem of false-positive, but there is a problem of weak photocurrent response (Peng et al., 2021; Hang et al., 2022). A two-electrode system with a photocathode as the working electrode and a photoanode as the reference/counter electrode was established to assist in enhancing the cathode signal, which is an effective way to solve the above problems (Ren et al., 2024).

Recently, many semiconductor nanomaterials have been applied to PEC sensors, including metal oxides and metal-sulfur compounds (Liu et al., 2019; Wu et al., 2018). However, individual semiconductor materials have low absorption efficiency of visible light and fast electron-hole (e^--h^+) pair recombination rates, leading to limitations in their practical applications (Nomellini et al., 2023; Wang et al., 2023). Researchers have addressed the shortcomings of single semiconductors by constructing energy band relationships between materials to form heterostructures(Chen et al., 2023; Mayes et al., 2023; Zhong et al., 2023). Among them, the Z-type heterostructure mechanism of the electron transfer allows the material to preserve strong oxidation and

* Corresponding author. Key Laboratory of Chemical Sensing & Analysis in Universities of Shandong, School of Chemistry and Chemical Engineering, University of Jinan, Jinan 250022, China.
** Corresponding author.
*** Corresponding author.
E-mail addresses: chenjingui1207@163.com (J. Chen), mse_zhaojx@ujn.edu.cn (J. Zhao), sdjndxwq@163.com (Q. Wei).

https://doi.org/10.1016/j.bios.2024.116387
Received 11 April 2024; Received in revised form 9 May 2024; Accepted 12 May 2024
Available online 13 May 2024

reduction properties, which reduces the recombination efficiency of e^{-}-h^{+}(Bu et al., 2023; Chen et al., 2023). $ZnIn_2S_4$ is a metal sulfide with simple synthesis and low cost(Zhang et al., 2023; Yang et al., 2023). Its narrow band gap of 2.4 eV makes it easy to realize electron jumping, but there is the problem of easy compounding of electron-hole pairs (Zhu et al., 2023; Wang et al., 2022). WO_3, as a metal oxide, has the advantages of easy preparation, high chemical stability and slight change in oxygen level by applying voltage (Azimirad et al., 2006; Gelija et al., 2023; Zhang et al., 2023). The band gap structure of WO_3 can form a Z-type heterostructure with $ZnIn_2S_4$, which accelerates the efficiency of electron transfer and inhibits the compounding of electron-hole pairs (Zhang et al., 2019). The combination of these two materials addresses the shortcomings of individual semiconductors and is a candidate for photoanodes (Liu et al., 2022). The P-type semiconductor material Co_3O_4 has a narrow bandgap and good visible light absorption characteristics. However, the low electron transfer rate limits its application in optics. Elemental doping is a common means to increase the electron transfer rate of semiconductors. Tungsten (W) partially doped with Co_3O_4 improves its photocurrent stability. In addition, the in situ reduction of gold nanoparticles ensures aptamer attachment. In addition, the localized plasmon resonance (LSPR) of the gold nanoparticles further allows for the fast transfer of electrons.

Herein, a self-powered photoelectrochemical aptamer sensor is proposed, Au@W–Co_3O_4 is used as the photocathode to provide a sensing interface, and $ZnIn_2S_4/WO_3$ is used as the photoanode to enhance the cathode signal for the highly sensitive detection of FB1. The dual-electrode operation mode solves the problem of the anti-interference ability of the photoanode and the low sensitivity of the cathode. In addition, the aptamer can sensitively recognize FB1, causing it to fall off the electrode surface, further realizing signal amplification.

2. Experimental section

2.1. The materials preparation process is reported in the supplementary material

2.1.1. Construction process of the PEC sensor

Scheme 1 shows the preparation and detection process of the PEC sensor. First, the preparation process of the photocathode is as follows. The Au@W–Co_3O_4 solution (30 μL, 4 mg/mL) is added dropwise to the ITO surface. After drying at room temperature, then add 10 μL of 1.0 μM c-DNA and incubate at room temperature. The electrode was then incubated with 6 μL of 1% bovine serum albumin (BSA) to block non-specific sites. Then, add 10 μL of 1.0 μM p-DNA and incubate at room temperature. Finally, different concentrations of FB1 were incubated on the surface of the electrode. The preparation process of the photoanode was as follows, $ZnIn_2S_4/WO_3$ solution (30 μL, 5 mg/mL) was added dropwise to the ITO surface.

3. Result and discussion

3.1. Characterization of $ZnIn_2S_4/WO_3$, and Au@W–Co_3O_4

The lattice compositions of $ZnIn_2S_4$, WO_3, and $ZnIn_2S_4/WO_3$ were analyzed by X-ray diffraction (XRD). As shown in Fig. 1A, $ZnIn_2S_4$ has five distinct diffraction peaks at 21.6°, 27.7°, 30.4,° 39.8°, and 47.2°, which are consistent with the crystal face of (0 0 6), (1 0 2), (1 0 4), (1 0 8), and (1 1 0) of $ZnIn_2S_4$ (PDF# 65–2023), which proves the successful synthesis of $ZnIn_2S_4$. WO_3 has six distinct diffraction peaks at 16.9°, 24.4°, 33.3,° 33.5°, 35.3°, and 53.5°, which are consistent with the crystal face of (1 1 0), (2 0 0), (0 2 2), (2 2 0), (1 2 2), and (0 2 4) of WO_3 (PDF# 43–1035), which proves the successful synthesis of WO_3 (Zhang et al., 2019). The diffraction peaks of the composite $ZnIn_2S_4/WO_3$ are in complete accordance with the diffraction peaks of $ZnIn_2S_4$ and WO_3. The successful synthesis of the $ZnIn_2S_4/WO_3$ was initially demonstrated. XRD spectrum (Fig. 1B) of Co_3O_4, which was able to correspond to cubic Co_3O_4 (PDF# 42–1467). The (3 1 1) crystal face of W–Co_3O_4 is shifted to the left against the (3 1 1) crystal face of Co_3O_4. The shift of the diffraction peaks to the left proves that W doping of Co_3O_4 induced internal structural changes (Song et al., 2023). The peaks at 38.3° and 44.6° correspond to the (1 1 1) and (2 0 0) crystal faces, proving the success of Au loading on the W–Co_3O_4 surface. Au loading and metal doping resulted in a faster electron transfer rate, which was confirmed by a subsequent comparison of the photocurrent response.

The synthesized materials were analyzed for elemental composition and elemental valence by X-ray photoelectron spectroscopy (XPS). The full spectrum of $ZnIn_2S_4/WO_3$ (Fig. S1A), in which all five elements Zn, In, S, W, and O were present. Figs. S1B–F show the high-resolution spectra of the five elements. Fig. S1B shows two peaks of Zn $2p_{3/2}$ and Zn $2p_{1/2}$ located at 1021.3 eV and 1044.5 eV, respectively, identifying the presence of Zn^{2+}. The positions at 445.6 eV and 452.1 eV are divided into two peaks (Fig. S1C), corresponding to In $3d_{5/2}$ and In $3d_{3/2}$. The two peaks of the element S correspond to the peaks in Fig. S1D for S $2p_{3/2}$ and S $2p_{1/2}$ at positions 161.3 eV and 162.3 eV, respectively. The two peaks of W belong to W $4f_{7/2}$ (34.8 eV) and W $4f_{5/2}$ (36.9 eV), as shown

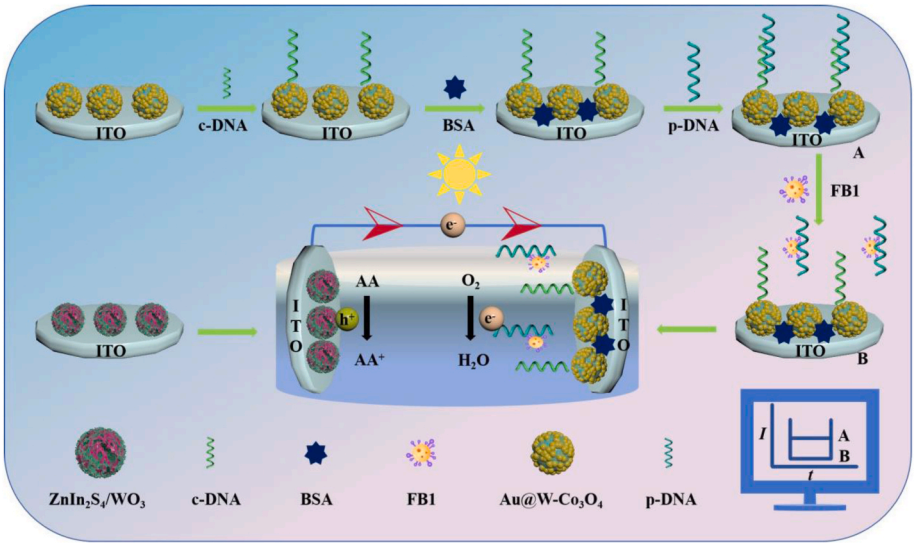

Scheme 1. PEC sensor construction process.

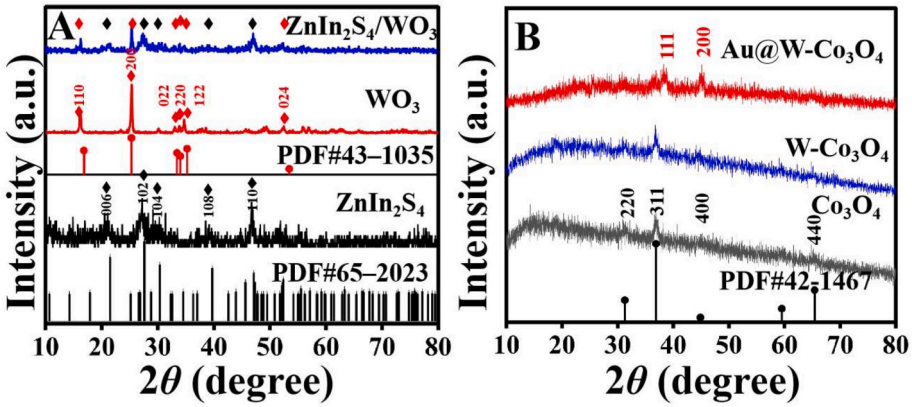

Fig. 1. (A) XRD patterns of $ZnIn_2S_4$, WO_3, and $ZnIn_2S_4/WO_3$, (B) XRD patterns of Co_3O_4, W–Co_3O_4, and Au@W–Co_3O_4.

in Fig. S1E. Finally, Fig. S1F shows the peaks of O 1s at 529.7 eV (OH^-) and 534.1 eV ($O_{vacancy}$). The above XPS analysis results proved that the preparation of $ZnIn_2S_4/WO_3$ nanocomposites was successful. Fig. S2A shows the XPS pattern of Au@W–Co_3O_4, in which Au, W, Co, and O are present. Table S1 shows the molar ratios of the elements in $ZnIn_2S_4/WO_3$, which also demonstrates the success of the material preparation. The positions at 83.7 eV and 87.3 eV are divided into two peaks (Fig. S2B), corresponding to Au $4f_{7/2}$ and Au $4f_{5/2}$. The two peaks of the element W correspond to the peaks in Fig. S2C for W $4f_{7/2}$ and W $4f_{5/2}$ at positions 34.2 eV and 36.3 eV, respectively. More specifically, the Co $2p_{3/2}$ region (Fig. S2D) showed two distinct peaks of Co^{3+} (779.3 eV) and Co^{2+} (781.1 eV). Additionally, the O 1s peak could be deconvoluted into two Gaussian peaks (Fig. S2E) corresponding to two oxygen states of O^{2-} (529.6 eV, defined as lattice oxygen), and O^{2-}(532.4 eV, defined as chemisorbed oxygen). The XPS analysis results proved that the preparation of Au@W–Co_3O_4 nanocomposites was successful.

Scanning electron microscopy (SEM) was used to analyze the prepared materials. Fig. 2A shows the SEM of WO_3, which was shaped as rectangular nanosheets with an average size of about 100 nm. As shown in Fig. 2B, $ZnIn_2S_4$ was a round ball composed of irregular petals with a diameter of about 4 μm. Fig. 2C and D were SEM images of $ZnIn_2S_4/WO_3$ with a diameter of about 4 μm. The WO_3 rectangular nanosheets were dispersed on the surface and inside of $ZnIn_2S_4$, forming new spheres and increasing the specific surface area (which is also confirmed by the comparison of specific surface areas below). The electronic energy spectrum (EDS) of $ZnIn_2S_4/WO_3$ (Fig. S3), in which the elements Zn, In, S, W, and O were present. Fig. 2E–I were the SEM electronic images and mapping of elements (Zn, In, S, W, and O) of $ZnIn_2S_4/WO_3$, respectively, with uniform elemental distribution. The successful preparation of $ZnIn_2S_4/WO_3$ was further proved. Fig. 3A was the SEM image of Co_3O_4, which was a nanoflower ball with a diameter of about 400 nm. Fig. 3B was an SEM image of W–Co_3O_4, a nanosphere with a smooth surface and a diameter of about 400 nm. Fig. 3C was an SEM image of Au@W–Co_3O_4 with Au nanoparticles attached to W–Co_3O_4 nanospheres. The EDS of Au@W–Co_3O_4 (Fig. S4), in which the elements Co, O, W, and Au were present. Fig. 3D–G were SEM electron images and mapping of elements (Co, O, W, and Au) of Au@W–Co_3O_4 with uniform elemental distribution. The successful preparation of Au@W–Co_3O_4 was proved.

3.2. Comparison of photocurrent, impedance, and surface active areas

The photocurrents of the materials, the photocurrents and

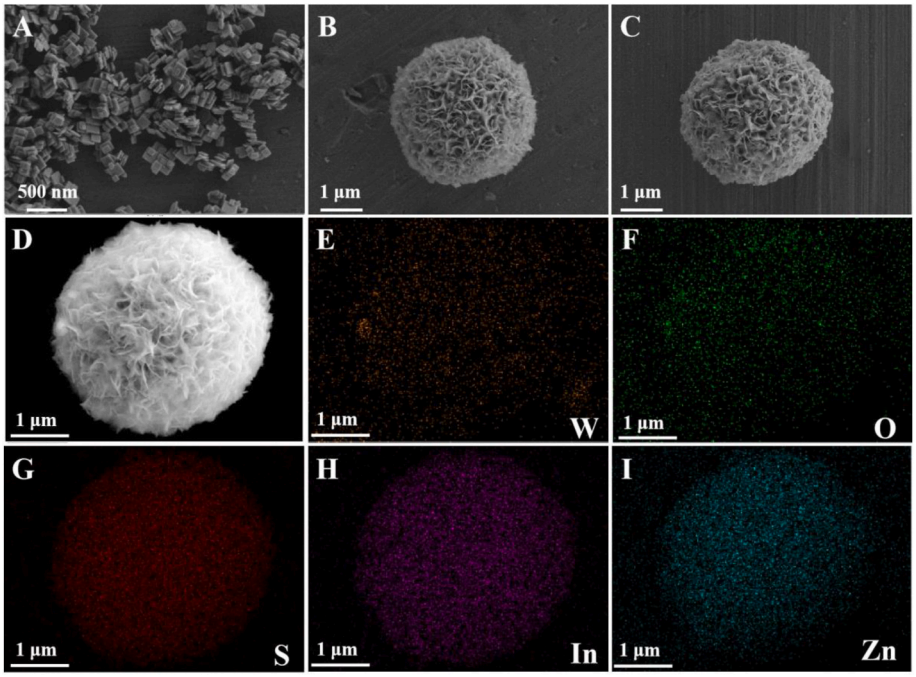

Fig. 2. (A) SEM image of WO_3, (B) SEM image of $ZnIn_2S_4$, (C) and (D) SEM image of $ZnIn_2S_4/WO_3$, (E–I) mapping images of $ZnIn_2S_4/WO_3$.

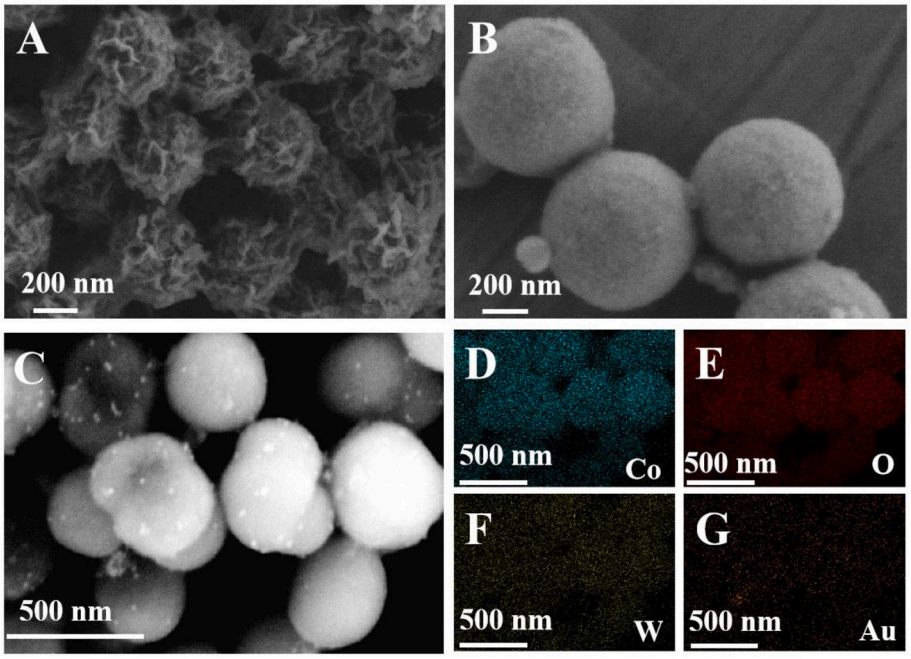

Fig. 3. (A) SEM of image Co_3O_4, (B) SEM image of W–Co_3O_4, (C) SEM image of Au@W–Co_3O_4, (D–G) mapping images of Au@W–Co_3O_4.

impedances of the sensor layer modifications, and the surface area of the materials were analyzed in comparison. Fig. S5A shows a comparison of the photoanode material currents, and curve a shows the photocurrent response of $ZnIn_2S_4$ (5.5 μA). Curve b was the photocurrent response of 9.9 μA for the composite material $ZnIn_2S_4/WO_3$ due to the accelerated electron transfer rate after forming a Z-type heterojunction between the two materials. Fig. S5B shows the photocurrent analysis before and after photocathode modification. Curve a shows the photocurrent response (−90 nA) at Co_3O_4, and curve b shows the photocurrent response (−150 nA) at W–Co_3O_4, which is due to the acceleration of the electron transfer rate by the doping of W (which creates defects). The LSPR effect of Au NPs elevated the electron activity and changed the photocurrent response to −250 nA (curve c). As shown in Fig. S5C, the photocathode current is 8.3 times higher in the presence of photoanode $ZnIn_2S_4/WO_3$. It is proved that the photoanode can self-enhance the photocathode current when no bias voltage is required.

Electrochemical impedance realities were performed to further demonstrate the success of the sensor layer modification. The specific experimental conditions were as follows: AC amplitude (5 mV), and frequency (0.1–100000 Hz). The test solution was one containing 0.1 M KCl and 5 mM $[Fe(CN)_6]^{4-/3-}$. Table S2 shows the four parameters of the circuit simulation including the electron transfer resistance (R_{et}), solution resistance (R_s), double layer capacitance (C_{dl}), and diffusion impedance (Z_w). Curve a in Fig. S5D was the R_{et} curve (18.4 Ω) of the bare ITO, which has excellent conductivity. After modifying Au@W–Co_3O_4, the R_{et} value increases to 54.06 Ω (curve b). The R_{et} value increases to 60.56 Ω due to the spatial site resistance effect of c-DNA (curve c). Modification of BSA for masking of non-specific sites increased R_{et} to 71.42 Ω (curve d). R_{et} increases to 99.82 Ω (curve f), which is a further increase in stereo-site blockade due to the specific binding of p-DNA and c-DNA. After modifying FB1, p-DNA detached into solution after binding to FB1, and R_{et} decreased to 80.93 Ω (curve e). In addition, the R_{et} of ITO/$ZnIn_2S_4/WO_3$ is 40.21 Ω (curve g). In conclusion, the impedance experiments reinforced that the modification of the PEC sensor was successful.

Finally, the electrode surface active areas of ITO, ITO/$ZnIn_2S_4/WO_3$, and ITO/Au@W–Co_3O_4 electrodes were compared (Chen et al., 2022). All calculations use the Randles Sevcik equation ($I = 2.69 \times 10^5$ A $D^{1/2}$ $n^{3/2}$ $v^{1/2}$ c). I is the peak current, A is electrically active surface area, D is the diffusion coefficient of $[Fe(CN)_6]^{4-/3-}$ of $(6.70 \pm 0.02) \times 10^{-6}$ cm^2/s, n is the number of electrons indicated to be transferred, c is the concentration value of $[Fe(CN)_6]^{4-/3-}$ of 5 mM, and v is the scanning rate (0.02 V/s - 0.2 V/s). Figs. S6A–C were CVs of ITO, ITO/$ZnIn_2S_4/WO_3$, and ITO/Au@W–Co_3O_4 at different scan rates with linear equations of $I = 1771 \times v^{1/2} + 38$ ($R^2 = 0.989$) (Fig. S6D), $I = 1929 \times v^{1/2} + 52$ ($R^2 = 0.994$) (Fig. S6E), and $I = 3388 \times v^{1/2} + 18$ ($R^2 = 0.997$) (Fig. S6F), respectively. The active areas were 0.50 cm^2 (ITO/$ZnIn_2S_4$), 0.56 cm^2 (ITO/$ZnIn_2S_4/WO_3$), and 0.98 cm^2 (ITO/, Au@W–Co_3O_4) respectively.

3.3. Optimization of PEC sensing conditions

To determine the optimal performance of the PEC sensor, the effects of substrate concentration, solution pH concentration, and ascorbic acid (AA) on the sensor were investigated. As shown in Figs. S7A–C, the photocurrent response reached its maximum value when the concentration of the substrate material was 5 mg/mL, the pH of the solution was 7.4, and the concentration of ascorbic acid was 0.1 mol/L.

3.4. Electron transport mechanism

The study of the electron transfer mechanism is a further analysis of how the sensor works (Chen et al., 2023a). The materials were tested for their ability to absorb visible light, and UV absorption tests were performed to calculate absorption edges for $ZnIn_2S_4$, WO_3, and W–Co_3O_4. As shown in Figs. S8A–C correspond to $ZnIn_2S_4$ (510 nm), WO_3 (498 nm), and W–Co_3O_4 (705 nm), respectively. The solid-state UV tests were performed through $ZnIn_2S_4$, WO_3, and W–Co_3O_4. The tested values in Figs. S8D–F correspond to the band gap width of $ZnIn_2S_4$ (2.42 eV), WO_3 (2.6 eV), and W–Co_3O_4 (1.72 eV), respectively. Figs. S8G–I were analyzed for the conduction or valence band positions of $ZnIn_2S_4$, WO_3, and W–Co_3O_4 using the Mott-Schottky test. The conduction band (E_{CB}) or the valence band (E_{VB}) were obtained for $ZnIn_2S_4$ ($E_{CB} = -0.92$ eV), WO_3 ($E_{CB} = 0.79$ eV), and W–Co_3O_4 ($E_{VB} = 1.36$ eV), respectively, and their conduction and valence bands were obtained as $ZnIn_2S_4$ ($E_{VB} = 1.50$ eV) after the formula $E_g = E_{VB} - E_{CB}$, respectively, WO_3 ($E_{CB} = 3.39$ eV) and W–Co_3O_4 ($E_{VB} = -0.36$ eV). On this basis, the possible electron transfer mechanism of the PEC sensor is explained. As shown in Fig. 4, under light, electrons are transferred from the conduction band of

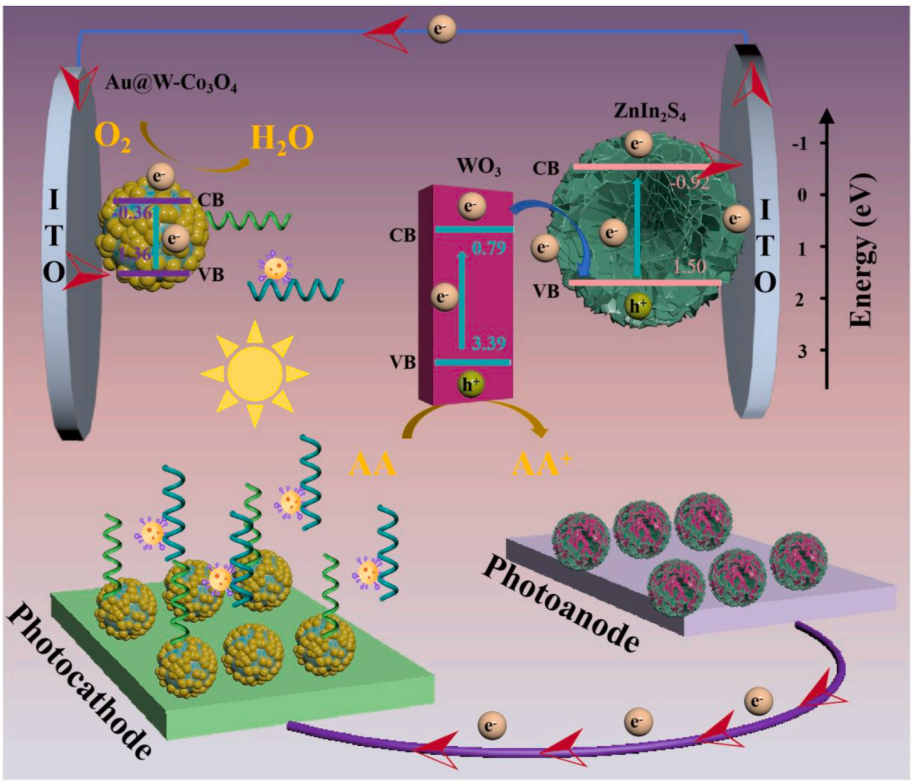

Fig. 4. Possible electron transfer mechanisms.

WO_3 to the valence band of $ZnIn_2S_4$, then to its conduction band, and continue to the photoanode. Electrons continue to be transferred from the outer circuit to the valence band of W–Co_3O_4 and to the conduction band of W–Co_3O_4 (the LSPR effect of gold nanoparticles accelerates electron transfer). Finally, the electrons in the conduction band of W–Co_3O_4 are captured by dissolved oxygen in solution. The holes in the valence band of tungsten trioxide are neutralized by ascorbic acid in the solution. After the above analysis, the working principle of the sensor can be understood more clearly.

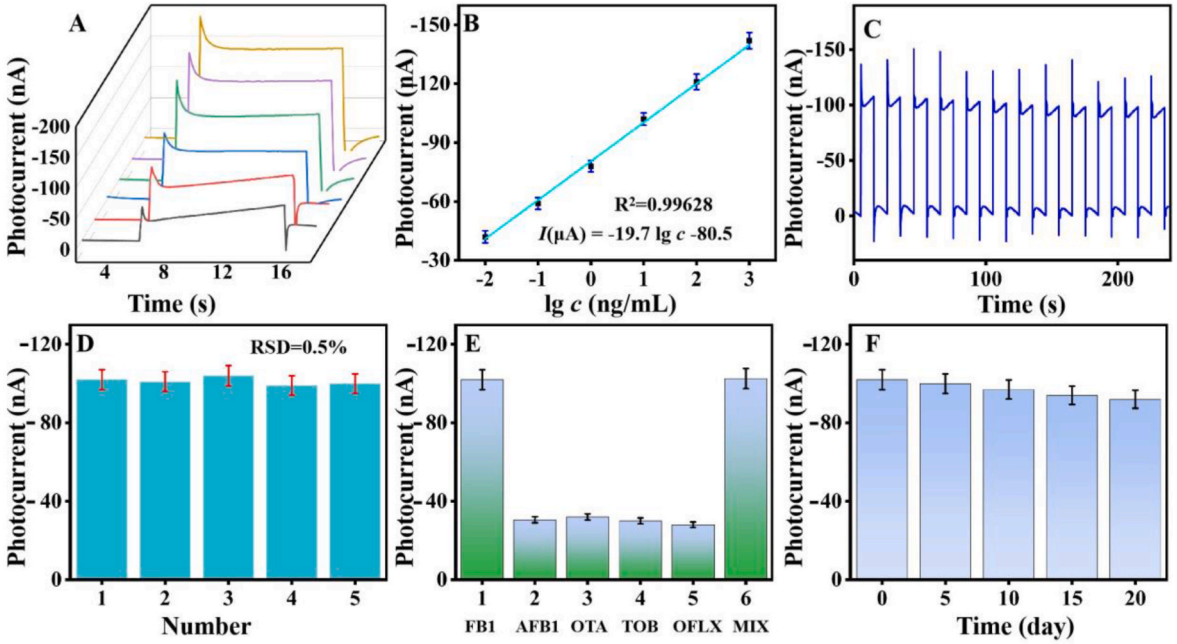

Fig. 5. (A) Photocurrent corresponding to different concentrations of FB1 (0.01, 0.1, 1, 10, 10^2, 10^3, ng/mL, error bar = SD, n = 5), (B) logarithmic calibration plot of the sensor at different concentrations of FB1 (error bar = SD, n = 5), (C) stability of the sensor (10 ng/mL of FB1), (D) reproducibility of the sensor (10 ng/mL); (E) photocurrent response of the sensor to FB1 (10 ng/mL), AFB1, OTA, TOB, OFLX, and mixtures of the five substances, and (F) storage stability of the sensor (10 ng/mL).

3.5. Performance of PEC sensor

Fig. 5A shows the *I-t* curves of the photocurrent of the sensor versus different concentrations (0.01, 0.1, 1, 10, 10^2, 10^3, ng/mL) of FB1. Fig. 5B shows the linear regression equation of *I* values versus the logarithm of FB1 concentration. It was observed that the sensor had a good linear relationship for FB1 between 0.01 - 10^3 ng/mL, and the linear regression equation was I (nA) = −19.7 lg c - 80.5 (R^2 = 0.995). The limit of detection of the PEC sensor was 2.7 pg/mL. In addition, the performance advantages and disadvantages of other detection methods were compared (Table S3). Finally, the photocurrent responses at different wavelengths at the same concentration were compared (Fig. S9). The results show that the light source has the largest photocurrent response in the range of 400–800 nm.

The test stability of the PEC sensor is one of the indicators to evaluate the sensor's goodness (Feng et al., 2021; Malmir and Fasihi, 2017). Therefore, the photocurrent change of the sensor was tested under 12 light switches at a FB1 concentration of 10 ng/mL of FB1. The results are shown in Fig. 5C, and the relative standard deviation of photocurrent does not exceed 2.6%. This PEC aptamer sensor has good test stability.

Reproducibility is an important basis to test whether the sensor is capable of repeated experiments (Bagi et al., 2024; Feng et al., 2020). Five identical sensors were prepared by different people in the same environment, and the reproducibility of the sensors was tested. As shown in Fig. 5D, the relative standard deviation (RSD) of the photocurrent values of the five sensors is 1.9%. The constructed PEC sensors were proved to have good reproducibility.

The selectivity of the sensors was evaluated. FB1, ochratoxin (OTA), tobramycin (TOB), and levofloxacin (OFLX) were used as interfering substances (Chen et al., 2023b). As shown in Fig. 5E, there is a significant difference in the photocurrent values between FB1 and other species, which is due to the selective recognition of p-DNA by FB1. The electrode currents modified by the mixture of the five substances were similar to those modified by FB1 alone, which proved that the sensor had a good anti-interference ability. Experiments show that the PEC sensor has good selectivity for the detection of FB1.

Storage stability is an important parameter for whether the sensor has test significance within a certain time range (Wu et al., 2023). The prepared PEC sensor was stored in a refrigerator at 4 °C for 20 days, and the photocurrent was tested every 5 days. As shown in Fig. 5F, the photocurrent values were 102 nA, 100 nA, 97 nA, 94 nA, and 92 μA, and the photocurrent value of the sensor in the fifth week decreased by 9.8% compared with the beginning. The prepared sensors have good storage capacity.

The accuracy of electrode currents was tested using anode and cathode materials as sensing interfaces, respectively. An oxidation reaction occurs at the anode and a reduction reaction occurs at the cathode. In actual samples, there may be a variety of reducing substances that cause a false positive reaction at the anode. To verify whether the cathode can reduce the probability of false positives, the following control experiment was conducted. Glutathione (GSH) was added to the PBS buffer to simulate the real sample environment. As shown in Figs. S10A and B, the RSD of the cathodic photocurrent is 2.8% in the absence of GSH and 1.7% in the presence of GSH. As shown in Figs. S10C and D, the RSD of the anodic photocurrent in the absence of GSH is 2.5% and the RSD of the anodic photocurrent in the presence of GSH is 8.5%. The results indicate that reducing substances affect the magnitude of the anodic photocurrent.

3.6. Real sample analysis

To test the sensor's ability to detect real samples, vinegar and soy sauce were recovered using the PEC method. A photograph of the detection process is shown in Fig. S11. Firstly, we conducted enzyme-linked immunosorbent assay testing, and the results showed that FB1 was not detected in both soy sauce and vinegar. Then we conducted spiked recovery experiments. As shown in Table S4, the recoveries in vinegar ranged from 97.1% to 103.2% with RSD of 3.4%–4.3%, the recoveries in soya sauce ranged from 98.7% to 101.5% with RSD of 3.7%–4.5%, and the recoveries in serum ranged from 97.9% to 102.5% with RSD of 2.5%–3.7%. Meanwhile, comparative experiments were performed with ELISA kits, and the results were similar to those of PEC. The PEC sensors had good performance in the testing of real samples.

4. Conclusions

In summary, a signal-amplified PEC self-powered aptamer sensor for FB1 detection was constructed. The cathode Au@W–Co_3O_4 was used as the sensing platform to solve the problem of a false-positive sensor. Z-type heterojunction $ZnIn_2S_4/WO_3$ greatly improved the photocurrent response of the cathode. What's more, the detection range of 10 pg/mL-1000 ng/mL has a good linearity with a detection limit of 2.7 pg/mL. Due to its aptamer-specific recognition, the sensor shows good working performance in the testing of real samples. This study opens up new avenues for the construction of PEC sensors and the specific PEC detection of FB1 in food samples.

Notes

The authors declare no competing financial interest.

CRediT authorship contribution statement

Xiang Ren: Writing – review & editing, Funding acquisition. **Jingui Chen:** Writing – original draft, Data curation. **Xiance Gan:** Data curation. **Na Song:** Data curation. **Xiaoran Yang:** Data curation. **Jinxiu Zhao:** Conceptualization. **Hongmin Ma:** Supervision. **Huangxian Ju:** Formal analysis. **Qin Wei:** Funding acquisition.

Declaration of competing interest

The authors declare that they have no known competing financial interests or personal relationships that could have appeared to influence the work reported in this paper.

Data availability

Data will be made available on request.

Acknowledgements

This study was supported by the National Natural Science Foundation of China (No. 22204059, 22274062), the Natural Science Foundation of Shandong Province (No. ZR2021QB120), the Excellent Youth Innovation Team of Higher Education Institutions in Shandong Province (2023KJ317), the Yunnan Provincial Key Laboratory of Rural Energy Engineering (Yunnan Normal University) Open Fund (2022KF007).

Appendix A. Supplementary data

Supplementary data to this article can be found online at https://doi.org/10.1016/j.bios.2024.116387.

References

Azimirad, R., Akhavan, O., Moshfegh, A.Z., 2006. J. Electrochem. Soc. 153 (2), E11–E16.
Bagi, M., Amjad, F., Ghoreishian, S.M., Sohrabi Shahsavari, S., Huh, Y.S., Moraveji, M.K., Shimpalee, S., 2024. BioChip J 18 (1), 45–67.
Bu, Y., Wang, K., Yang, X., Nie, G., 2023. Biosens. Bioelectron. 237, 115507.
Chen, J., Song, N., Zhang, N., Gao, Z., Wu, D., M, H., Ren, X., Wei, Q., 2023a. Chem. Eng. J. 473, 145276.
Chen, J., Zhao, J., Feng, J., Wu, D., Ma, H., Ren, X., Wei, Q., Ju, H., 2022. Anal. Chem. 94 (50), 17396–17404.

Chen, J., Zhao, J., Feng, R., Ma, H., Wang, H., Ren, X., Wei, Q., Ju, H., 2023b. J. Hazard Mater. 459, 132122.
Chen, X., Huang, H., Wu, Q., Xue, F., Zhao, Z., Liu, J., Duan, H., Chen, H., 2023c. Anal. Chim. Acta 1283, 341940.
Chen, X., Wu, W., Zeng, J., Ibanez, E., Cifuentes, A., Mao, J., Yu, L., Wu, H., Li, P., Zhang, Z., 2023d. J. Hazard Mater. 460, 132281.
Feng, J., Li, N., Du, Y., Ren, X., Wang, X., Liu, X., Ma, H., Wei, Q., 2021. Anal. Chem. 93 (42), 14196–14203.
Feng, J., Qian, Y., Cheng, Q., Ma, Y., Wu, D., Ma, H., Ren, X., Wang, X., Wei, Q., 2020. Biosens. Bioelectron. 168, 112503.
Gelija, D., Loka, C., Goddati, M., Bak, N.H., Lee, J., Kim, M.D., 2023. ACS Appl. Mater. Interfaces 15 (29), 34883–34894.
Govindaraju, G.V., Wheeler, G.P., Lee, D., Choi, K.-S., 2016. Chem. Mater. 29 (1), 355–370.
Hang, T., Li, C., Liang, D., Li, S., Zhou, H., Ge, P., Zhu, X., Liu, T., 2022. Chem. Eng. J. 431, 133465.
Liu, C., Mao, S., Wang, H., Wu, Y., Wang, F., Xia, M., Chen, Q., 2022. Chem. Eng. J. 430, 132806.
Liu, C., Meng, F., Zhang, L., Zhang, D., Wei, S., Qi, K., Fan, J., Zhang, H., Cui, X., 2019. Appl. Surf. Sci. 469, 276–282.
Malmir, N., Fasihi, K., 2017. J. Mod. Opt. 64 (20), 2195–2200.
Mao, L., Ji, K., Yao, L., Xue, X., Wen, W., Zhang, X., Wang, S., 2019. Biosens. Bioelectron. 127, 57–63.
Mayes, M., Farahmand, F., Grossnickle, M., Lohmann, M., Aldosary, M., Li, J., Aji, V., Shi, J., Song, J.C.W., Gabor, N.M., 2023. Proc. Natl. Acad. Sci. U.S.A. 120 (39), e2221815120.
Nomellini, C., Polo, A., Mesa, C.A., Pastor, E., Marra, G., Grigioni, I., Dozzi, M.V., Gimenez, S., Selli, E., 2023. ACS Appl. Mater. Interfaces 15 (45), 52436–52447.
Peng, B., Zhang, Z., Tang, L., Ouyang, X., Zhu, X., Chen, L., Fan, X., Zhou, Z., Wang, J., 2021. Anal. Chem. 93 (26), 9129–9138.
Ren, X., Song, N., Chen, J., Gao, M., Wang, H., Gao, Z.F., Ju, H., Zhao, J., Wei, Q., 2024. Talanta 272, 125780.
Shu, J., Tang, D., 2020. Anal. Chem. 92 (1), 363–377.
Song, L., Xu, L., Ahn, J., Baek, J.W., Kim, I.D., 2023. ACS Sens. 8 (9), 3417–3427.
Sun, J., He, Y., He, S., Liu, D., Lu, K., Yao, W., Jia, N., 2022. Biosens. Bioelectron. 204, 114056.
Wang, F., Ding, Q., Ding, J., Bai, Y., Bai, H., Fan, W., 2022. Chem. Eng. J. 450, 138260.
Wang, H., Gao, R.T., Nguyen, N.T., Bai, J., Ren, S., Liu, X., Zhang, X., Wang, L., 2023. ACS Nano 17 (21), 22071–22081.
Wei, J.J., Wang, G.Q., Zheng, J.Y., Yang, H.Y., Wang, A.J., Mei, L.P., Feng, J.J., Cheang, T.Y., 2023. Biosens. Bioelectron. 230, 115293.
Wu, P., Liu, Z., Chen, D., Zhou, M., Wei, J., 2018. Appl. Surf. Sci. 440, 1101–1106.
Wu, T., Du, Y., Gao, Z., Xu, K., Dai, L., Liu, L., Li, F., Wei, Q., Ju, H., 2023. Anal. Chem. 95 (2), 1627–1634.
Yang, H.Y., Wei, J.J., Zheng, J.Y., Ai, Q.Y., Wang, A.J., Feng, J.J., 2023. Talanta 260, 124631.
Zang, Y., Fan, J., Ju, Y., Xue, H., Pang, H., 2018. Chemistry 24 (53), 14010–14027.
Zhang, B., An, Z., Li, M., Guo, L.-H., 2023a. TrAC, Trends Anal. Chem. 165, 117149.
Zhang, B., Wang, H., Xi, J., Zhao, F., Zeng, B., 2019. Sens. Actuators, B 298, 126835.
Zhang, L., Zhang, Z., Liu, R., Wang, S., Li, L., Zhao, P., Wang, Y., Ge, S., Yu, J., 2023b. Sens. Actuators, B 394, 134334.
Zhao, C.-Q., Ding, S.-N., 2019. Coord. Chem. Rev. 391, 1–14.
Zhong, C., Zhang, C., Yang, Y., Liang, X., Pang, Q., Zhou, L., Chen, P., 2023. Food Chem. 437, 137877.
Zhu, L.B., Wang, H.Y., Zhang, T.Y., Chen, F.Z., Han, D.M., Zhao, W.W., 2021. Anal. Chem. 93 (47), 15761–15767.
Zhu, Y., Ju, P., Wang, S., Jiang, T., Chi, J., Zhang, S., Zhai, X., Lu, Z., 2023. Anal. Chim. Acta 1240, 340757.